Research Square

Preprints are preliminary reports that have not undergone peer review.
They should not be considered conclusive, used to inform clinical practice,
or referenced by the media as validated information.

ATF2 drives macrophage-mediated anti-PD-1 resistance by coupling KAT3A-dependent H3K18 lactylation with CCL2 transcription in hepatocellular carcinoma

Yucheng Hou

Houych05@ustc.edu.cn

the University of Science and Technology of China https://orcid.org/0000-0003-2569-1680

Conghuan Shen

Huashan hospital

Changjie Yang

Renji Hospital, Shanghai Jiao Tong University School of Medicine

Fangqi Ma

The First Affiliated Hospital of USTC, Division of Life Sciences and Medicine, University of Science and Technology of China

Ensi Ma

Huashan Hospital & Institute of Organ Transplantation, Fudan University

Hongyuan Xue

Huashan hospital

Chao Sun

Huashan Hospital & Institute of Organ Transplantation, Fudan University

Li Li

Huashan Hospital

Jianhua Li

Huashan hospital

ruipeng song

University of Science and Technology of China (USTC) https://orcid.org/0000-0002-1912-3735

Qing Wang

Zhongshan Hospital, Fudan University

Jizhou Wang

The First Affiliated Hospital of USTC

Zhengxin Wang

Huashan Hospital

Article

Keywords: ATF2, hepatocellular carcinoma, M2 macrophages, CCL2, histone lactylation, KAT3A, NF-κB, PD-1 resistance, immunotherapy

Posted Date: August 25th, 2026

DOI: https://doi.org/10.21203/rs.3.rs-10533707/v1

License: This work is licensed under a Creative Commons Attribution 4.0 International License. Read Full License

Additional Declarations: (Not answered)

ATF2 drives macrophage-mediated anti-PD-1 resistance by coupling KAT3A-dependent H3K18 lactylation with CCL2 transcription in hepatocellular carcinoma

Conghuan Shen[1,#], Yuchen Hou[2,3,4,#], Changjie Yang[5,#], Fangqi Ma[6,#], Ensi Ma[1,2], Hongyuan Xue[1,2], Chao Sun[1,2], Li Li[1,2], Jianhua Li[1,2], Ruipeng Song[2,3,4,*],Qing Wang[7], Jizhou Wang[2,3,4,*], Zhengxin Wang[1,*, §]

Affiliation:

1. Liver Transplantation Center, Department of General Surgery, Huashan Hospital & Institute of Organ Transplantation, Fudan University, Shanghai 200040, China.

2. Department of Hepatobiliary Surgery, the First Affiliated Hospital of USTC, Division of Life Sciences and Medicine, University of Science and Technology of China, Hefei, Anhui, 230001, P.R. China.

3. Anhui Province Key Laboratory of Hepatopancreatobiliary Surgery, Hefei, Anhui, P.R. China.

4. Anhui Provincial Clinical Research Center for Hepatobiliary Diseases, Hefei, Anhui, P.R. China.

5. Department of Gastrointestinal Surgery, Renji Hospital, Shanghai Jiao Tong University School of Medicine, Shanghai, 200120, P.R. China

6. Department of Traditional Chinese Medicine, the First Affiliated Hospital of USTC, Division of Life Sciences and Medicine, University of Science and Technology of China, Hefei, Anhui, 230001, P.R. China.

7. Department of Medical Oncology, Zhongshan Hospital, Fudan University, Shanghai, 200032, P.R. China.

[#] These authors contribute equally to this work.

[§] Lead contact

***Correspondence to:**

Zhengxin Wang (wangzhengxin@huashan.org.cn), Liver Transplantation Center, Department of General Surgery, Huashan Hospital, Fudan University, Shanghai, 200040, P. R. China.

Jizhou Wang (wangjoe@ustc.edu.cn), Department of Hepatobiliary Surgery, the First Affiliated Hospital of USTC, Division of Life Sciences and Medicine, University of Science and Technology of China, Hefei, Anhui, 230001, P.R. China.

Qing Wang (wang.qing2@zs-hospital.sh.cn), Department of Medical Oncology, Zhongshan Hospital, Fudan University, Shanghai, 200032, P.R. China.

Ruipeng Song (songruipeng@ustc.edu.cn), Department of Hepatobiliary Surgery, the First Affiliated Hospital of USTC, Division of Life Sciences and Medicine, University of Science and Technology of China, Hefei, Anhui, 230001, P.R. China.

Ethics approval and consent to participate

All clinical samples were approved by the Huashan Hospital Institutional Review Board, Fudan University (2021-856). All animal experiments were approved by the Institutional Animal Care and Use Committee of Fudan University (202311014S).

Competing interests

The authors declare no competing interests.

Funding

This study was supported by the National Key Research and Development Program of China (2023YFC2505900), the National Natural Science Foundation (82241225, 82572040, 82303863 and 82505109), the China Postdoctoral Science Foundation

(2023M733389), the Youth Program of the Anhui Provincial Natural Science Foundation (2508085QH347).

Authors' contribution

C.S., Y.H., R.S., J.W. and Z.W. conceived and designed the study. Y.H. and F.M. performed epigenomic sequencing experiments, including ChIP-seq, ATAC-seq, and integrative multi-omics analyses, and participated in data interpretation. C.Y. mainly conducted animal experiments, including orthotopic tumor models and in vivo functional validation. E.M., H.X., C.Su., L.L., and J.L. performed in vitro functional assays, molecular biology experiments, and assisted with data collection. R.S., J.W. and Z.W. supervised the study and provided critical guidance on experimental design and data analysis. C.S. and Y.H. drafted the manuscript. All authors contributed to data discussion, manuscript revision, and approved the final version.

Data Availability Statement

The data generated in this study, including bulk RNA-seq, ATAC-seq, ChIP-seq, RNA-seq, GRO-seq, processed sequencing data, source data for figures, and other de-identified experimental data, are available from the corresponding authors upon reasonable request.

Abstract

Immune checkpoint blockade has improved the treatment of hepatocellular carcinoma (HCC), yet most patients fail to achieve durable responses to PD-1 blockade. Tumor-associated macrophages are major determinants of immunotherapy resistance, but the tumor-intrinsic epigenetic programs that recruit and polarize macrophages in HCC remain incompletely defined. Here, we identify activating

transcription factor 2 (ATF2) as a driver of macrophage-mediated PD-1 resistance in HCC. Integrated single-cell and spatial transcriptomic analyses revealed enrichment of M2-like macrophages in non-responding tumors and identified ATF2 as a candidate tumor-intrinsic regulator associated with this immunosuppressive state. Genetic perturbation of ATF2 in syngeneic HCC models demonstrated that ATF2 promotes tumor growth, M2-like macrophage accumulation, $CD8^+$ T-cell dysfunction, and resistance to PD-1 blockade. Mechanistically, ATF2 enhanced CCL2-dependent macrophage recruitment and polarization by coupling transcriptional activation with enhancer remodeling. ATF2 interacted with KAT3A/CBP to increase global and site-specific histone lactylation, particularly H3K18 lactylation, thereby preserving chromatin accessibility at NF-κB-responsive regulatory elements and sustaining inflammatory and chemokine transcription. ATF2 also directly bound the CCL2 promoter, establishing a dual mechanism for CCL2 activation. Pharmacologic inhibition of ATF2 remodeled the tumor immune microenvironment, reduced $CD206^+$ macrophage infiltration, restored $CD8^+$ T-cell effector function, and sensitized orthotopic HCC tumors to PD-1 blockade without overt toxicity. In patient specimens, elevated ATF2 and H3K18 lactylation correlated with NF-κB target expression, $CD206^+$ macrophage enrichment, reduced $CD8^+$ T-cell infiltration, and non-response to anti-PD-1 therapy. These findings define an ATF2-KAT3A-H3K18la-NF-κB chemokine axis that promotes macrophage-mediated immune evasion and nominate ATF2 as a therapeutic target for overcoming PD-1 resistance in HCC.

Keywords: ATF2, hepatocellular carcinoma, M2 macrophages, CCL2, histone lactylation, KAT3A, NF-κB, PD-1 resistance, immunotherapy

Introduction

Hepatocellular carcinoma (HCC) remains a leading cause of cancer-related mortality worldwide, and its incidence continues to rise despite advances in surveillance and clinical management [1, 2]. Immune checkpoint blockade (ICB), particularly anti-programmed cell death protein-1 (αPD-1) therapy, has reshaped the therapeutic landscape for advanced HCC. However, only a minority of patients achieve durable responses, and resistance to αPD-1 therapy represents a major clinical challenge [3-5]. Increasing evidence indicates that the tumor immune microenvironment (TME), rather than tumor-intrinsic factors alone, plays a decisive role in determining responsiveness to immunotherapy [6, 7]. Therefore, defining the key tumor-intrinsic regulators that remodel the immunosuppressive TME is essential for improving the efficacy of anti-PD-1 blockade in HCC.

Among immune cells in the TME, tumor-associated macrophages (TAMs) are particularly abundant and exert profound immunoregulatory effects. TAMs can be broadly classified into classically activated M1 macrophages, which display pro-inflammatory and anti-tumor activities, and alternatively activated M2 macrophages, which promote angiogenesis, tumor growth, and immune suppression [8]. In HCC, TAMs frequently acquire an M2-like phenotype characterized by immunosuppressive signaling, enhanced tumor progression, and inhibition of cytotoxic T-cell activity [9-11]. High intratumoral M2 macrophage infiltration correlates strongly with poor prognosis and diminished responsiveness to αPD-1 treatment [12-14]. Recent multi-omics studies further suggest that dynamic crosstalk between tumor cells and TAMs is essential in establishing an immunosuppressive milieu that facilitates immune evasion and therapeutic failure [15-17]. Several tumor-intrinsic factors, including CSF1, HMGB1, and RNase1, have been shown to promote macrophage M2 polarization and immune escape [18, 19]. Nevertheless, the upstream mechanisms by which HCC cells coordinate macrophage recruitment and polarization in anti-PD-1-resistant tumors remain incompletely defined.

Activating transcription factor 2 (ATF2), a stress-responsive transcription factor

implicated in inflammation, oncogenesis, and chromatin remodeling, has emerged as a potential modulator of tumor-immune interactions [20, 21]. Although ATF2 has been linked to tumor progression in several malignancies, its role in orchestrating macrophage-mediated immunosuppression in HCC remains largely unexplored. Previous studies have shown that ATF2 can regulate gene transcription through histone modification-associated mechanisms, including interactions with histone acetyltransferases such as KAT3A/CBP [22, 23]. Given the importance of epigenetic reprogramming in immune resistance, ATF2 may represent a crucial upstream regulator that couples tumor-intrinsic chromatin states to macrophage behavior within the TME.

Chemokine CCL2 is a well-established driver of monocyte recruitment and M2 macrophage polarization in HCC and other solid tumors [24-26]. Although CCL2 upregulation is frequently observed in immunotherapy-resistant tumors, the upstream pathways controlling its expression in resistant HCC remain to be fully defined. Whether ATF2 directly regulates CCL2 transcription and thereby shapes macrophage infiltration has not been determined. In addition, histone lactylation, a recently identified epigenetic modification derived from lactate, has emerged as an important regulator of macrophage polarization and tumor progression [27, 28]. In particular, H3K18 lactylation (H3K18la) has been associated with transcriptional activation in metabolically reprogrammed TMEs [29, 30]. However, the regulatory machinery controlling H3K18la in HCC and its potential connection to ATF2-dependent immune resistance remain unclear.

In the present study, we integrated single-cell transcriptomics, spatial transcriptomics, epigenomic profiling, and functional immunological assays to identify ATF2 as a tumor-intrinsic driver of anti-PD-1 resistance in HCC. We demonstrate that ATF2 is elevated in anti-PD-1-resistant tumors with high M2 macrophage infiltration, promotes CCL2-dependent macrophage recruitment and polarization, and enhances global and site-specific histone lactylation, particularly H3K18la, through cooperation with KAT3A. Mechanistically, the ATF2-KAT3A-H3K18la axis preserves enhancer accessibility at

NF-κB-responsive regulatory elements, thereby sustaining transcription of immunosuppressive chemokine and inflammatory genes such as CCL2. Pharmacological inhibition of ATF2 remodels the TME, restores $CD8^+$ T-cell function, and markedly improves the therapeutic response to anti-PD-1 therapy in preclinical HCC models. Together, these findings identify ATF2 as a central regulator of macrophage-mediated immunosuppression and a promising therapeutic target for overcoming immune checkpoint blockade resistance in HCC.

Results

ATF2 is elevated in αPD-1-Resistant HCC with high M2 infiltration

To comprehensively characterize the immune landscape of HCC, we integrated single-cell RNA sequencing (scRNA-seq) datasets from three independent public cohorts (CRA002308, GSE149614 and GSE242889), comprising a total of 44,683 cells from 38 samples (**Figure 1A-B**). Unsupervised clustering delineated 11 major myeloid subtypes, including multiple macrophage and monocyte subsets, dendritic cell (DC) populations, plasmacytoid DCs (pDCs), and neutrophils (**Figure 1C**; Figure S1A). Comparative analysis between tumor and adjacent normal (AN) tissues demonstrated a significant enrichment of $SPP1^+$ and $APOH^+$ macrophages within tumor samples (**Figure 1D**). Notably, TAMs exhibited a markedly higher M2 polarization score and a significantly lower M1 polarization score compared to those from adjacent tissues, indicating a predominance of immunosuppressive phenotypes within the TME (**Figure 1E**; Figure S1B). Consistently, spatial transcriptomic analysis demonstrated that M2 macrophages were predominantly localized within tumor regions of αPD-1 non-responsive patients, whereas responsive patients exhibited markedly reduced M2 macrophage infiltration (**Figure 1F**). Collectively, these data suggest that M2 macrophages play a crucial role in shaping an immunosuppressive TME that contributes to αPD-1 resistance in HCC.

To further identify key regulators driving M2 macrophage infiltration, we performed

bulk RNA sequencing on M2Φ^{high} and M2Φ^{low} HCC tissues (**Figure 1G**). Integration of differentially expressed genes (DEGs) from the M2Φ^{high} versus M2Φ^{low} HCC comparison, together with tumor versus normal transcriptomic data from TCGA and GEO datasets, revealed seven overlapping candidate genes (*ATF2*, *GNPDA1*, *PALLD*, *CDK4*, *MAPRE1*, *TEAD2* and *UBE2Q2*) potentially involved in regulating M2 macrophage polarization (**Figure 1H**; Figure S1C-D). RT-qPCR validation confirmed that ATF2 was significantly upregulated in αPD-1-resistant HCC samples (**Figure 1I**). Moreover, αPD-1-resistant tumors displayed elevated ATF2 expression accompanied by increased infiltration of CD206^{+}CD11b^{+} macrophages and reduced CD8^{+} T-cell abundance (**Figure 1J**). In agreement, immunohistochemical analysis demonstrated higher ATF2 expression in advanced-stage HCC tissues compared with early-stage counterparts (Figure S1E). Together, these findings indicate that ATF2 is upregulated in αPD-1-resistant HCC, and its elevated expression is positively correlated with enhanced M2 macrophage infiltration and the establishment of an immunosuppressive tumor microenvironment.

ATF2 promotes M2-like polarization and tumorigenesis in HCC

As previously reported, the TME of the TIBx syngeneic HCC model is resistant to αPD-1 therapy and contains a high proportion of M2-like TAMs[31]. Therefore, we knocked out ATF2 in TIBx cells to investigate its regulatory role in M2 macrophage polarization (**Figure 2A**). Immunohistochemistry (IHC) confirmed that ATF2 was effectively deleted in TIBx cells (Figure S2B). Tumorigenesis assays showed that ATF2 knockout significantly reduced tumor size, whereas adoptive transfer of M2 macrophages restored tumor growth (**Figure 2B**). Flow cytometry was used to analyze macrophage polarization in tumor tissues from different experimental groups and the gating strategy was shown in Figure S2A. Flow cytometry results demonstrated that ATF2 knockout markedly decreased the proportion of M2 macrophages while increasing the proportion of M1 macrophages. Following adoptive transfer of M2 macrophages, the infiltration of M2 macrophages in tumor tissues was

significantly increased (**Figure 2C-D**). Moreover, ATF2 knockout substantially enhanced $CD8^+$ T-cell infiltration and elevated GZMB and IFN-γ levels, while reducing $CD8^+$ T-cell exhaustion markers. Conversely, adoptive transfer of M2 macrophages suppressed $CD8^+$ T-cell activity and increased exhaustion marker expression (**Figure 2E-F**, Figure S2C). Immunofluorescence further confirmed that $CD206^+CD11b^+$ macrophages were significantly decreased and $CD8^+$ T-cell infiltration increased after ATF2 knockout, while adoptive transfer of M2 macrophages led to the opposite effect, with increased $CD206^+$ $CD11b^+$ macrophages and decreased $CD8^+$ T-cell infiltration (**Figure 2G**).

Subsequently, we overexpressed ATF2 in the Hepa 53.4 syngeneic hepatocellular carcinoma (HCC) model[31], which is characterized by low M2 macrophage infiltration (**Figure 2H**, Figure S2D). The results showed that ATF2 overexpression markedly promoted tumor growth, while treatment with the M2 macrophage inhibitor GW2580 reversed this effect (**Figure 2I**). Flow cytometry analysis revealed that ATF2 overexpression significantly increased the proportion of M2 macrophages and reduced M1 macrophages, whereas GW2580 treatment effectively suppressed M2 macrophage infiltration (**Figure 2J-K)**. Furthermore, ATF2 overexpression significantly inhibited $CD8^+$ T-cell infiltration and reduced GZMB and IFN-γ levels, while upregulating $CD8^+$ T-cell exhaustion markers. Treatment with GW2580, however, reactivated $CD8^+$ T-cell function and reduced exhaustion marker expression (**Figure 2L-M**, Figure S2E). Multicolor immunofluorescence also demonstrated that ATF2 overexpression increased $CD206^+CD11b^+$ macrophage numbers and reduced $CD8^+$ T-cell infiltration, while GW2580 treatment reversed these changes, leading to reduced $CD206^+CD11b^+$ macrophages and increased $CD8^+$ T-cell infiltration (Figure 2N). Collectively, these results indicate that ATF2 promotes the formation of an immunosuppressive tumor microenvironment in HCC primarily by regulating M2 macrophage polarization.

ATF2 activates an NF-κB chemokine program in which CCL2 functions as a key

macrophage-recruiting effector

To further investigate how tumor cell-intrinsic ATF2 influences macrophage behavior, we developed an in vitro co-culture model combining HCC cells with macrophages (**Figure 3A**). Both gain- and loss-of-function experiments revealed that ATF2 silencing in HCC cells suppressed, whereas ATF2 overexpression enhanced, macrophage M2-like polarization and migration. This was indicated by changes in transcriptional alterations in M1-associated genes (NOS2, CXCL10, CXCL9, TNF-α) and M2-associated genes (CD206, CD163, ARG1, TGF-β1, IL-10) (**Figure 3B-C**, Figure S3A-B). Furthermore, supernatants from co-cultures with ATF2-knockdown $ATF2^{high}$ HCC cells (Huh7 and SNU-387) reduced macrophage migration, whereas supernatants from co-cultures with ATF2-overexpressing $ATF2^{low}$ HCC cells (SNU475 and JHH-4) enhanced macrophage migration (**Figure 3D-E**, Figure S3C-D). Collectively, these findings demonstrate that ATF2 modulates macrophage recruitment and M2-like polarization in HCC, thereby contributing to the formation of an immunosuppressive TME.

After confirming that ATF2 is crucial in modulating macrophage function, we sought to determine the key downstream factor mediating this regulation. RT-qPCR analysis of cytokine profiles in supernatants from ATF2-knockdown and control Huh7 cells revealed that CCL2 exhibited the most pronounced down-regulation following ATF2 depletion (**Figure 3F**), which was further validated by ELISA results (**Figure 3G**). Given that CCL2 has been implicated in enhancing tumor-associated macrophage (TAM) infiltration and promoting M2 polarization in HCC [32, 33], we next examined whether CCL2 serves as the intermediary between tumor-intrinsic ATF2 and macrophage polarization. Consistent with this hypothesis, CCL2 knockdown in ATF2-overexpressing $ATF2^{low}$ HCC cells (SNU475 and JHH-4) markedly reduced macrophage migration and M2-like polarization, whereas restoration of CCL2 expression in ATF2-knockdown $ATF2^{high}$ HCC cells (Huh7 and SNU-387) effectively reversed the macrophage phenotypic alterations induced by ATF2 loss (**Figure 3H-J**, Figure S3E-H). Taken together, these findings demonstrate that HCC cell-intrinsic

ATF2 modulates macrophage M2-like polarization through a CCL2-dependent mechanism.

ATF2 couples KAT3A-dependent H3K18la to immunosuppressive chemokine activation

To investigate how ATF2 exerts its biological functions, we first examined global lactylation levels in patients with high versus low ATF2 expression. The results showed that patients with high ATF2 expression exhibited markedly elevated global lactylation (**Figure 4A**). Consistently, Western blot analysis demonstrated that the overall lactylation level was substantially higher in five tumors from anti-PD-1-resistant patients compared with those from responders (**Figure 4B**). The overall lactylation level was significantly decreased in ATF2 knockdown HCC cells (Figure S4A). Further lactylation-specific Western blotting in ATF2-overexpressing SNU-475 cell lines revealed that not only global lactylation but also multiple individual lactylation sites,including H3K18la, H3K9la, H3K14la, and H4K12la, were significantly increased, with H3K18la showing the most pronounced change (**Figure 4C**).

We next performed ChIP-seq analysis of these lactylation marks together with ATF2. The results showed that H3K18la exhibited the highest degree of genome-wide co-localization and distributional concordance with ATF2, compared with the other lactylation sites (**Figure 4D**). Interestingly, molecular docking predictions suggested that there is no clear physical docking interface between ATF2 and H3K18la (Figure S4B). In addition, ITC assays using purified proteins showed that ATF2 displayed no significant difference in binding affinity between lactylated and non-lactylated H3K18 peptides (**Figure 4E**). These findings indicate that ATF2 is unlikely to directly recognize or catalyze histone lactylation.

We then assessed the relationship between expression levels of canonical and non-canonical histone lactylation “writer” enzymes, including members of the KAT family, and H3K18la enrichment. The results revealed that reduced expression of

KAT3A significantly decreased H3K18la levels (Figure S4C). Co-immunoprecipitation further demonstrated that ATF2 physically interacts with KAT3A (**Figure 4F**). Moreover, ATAC-seq and ChIP-seq analyses showed that KAT3A knockdown markedly decreased chromatin accessibility, exhibited genome-wide co-enrichment with ATF2, and profoundly affected ATF2 chromatin occupancy (**Figure 4G-I**). Collectively, these findings demonstrate that ATF2 promotes global and site-specific histone lactylation, particularly H3K18la, by cooperating with KAT3A to regulate transcriptional activity.

ATF2 maintains NF-κB enhancer accessibility to sustain inflammatory chemokine transcription

To investigate how ATF2, functioning as a potential chromatin-associated transcriptional organizer, influences chromatin remodeling, we performed integrated RNA-seq and ATAC-seq analyses. KEGG and GSEA of the RNA-seq data revealed that ATF2 knockdown significantly enriched differentially expressed genes (DEGs) in multiple signaling pathways, including the NF-κB pathway (**Figure 5A-C**). Notably, qPCR validation confirmed that several downstream targets of p65, such as CCL2, were markedly downregulated at the mRNA level upon ATF2 depletion (**Figure 5D**). Consistent with these transcriptomic changes, ATAC-seq comparing chromatin accessibility between ATF2-knockdown and control cells showed a substantial loss of open chromatin regions. Specifically, 32,556 peaks were closed out of a total of 99,759 peaks following ATF2 knockdown (**Figure 5E**). Clustering analysis of promoter-associated peaks within this closed-chromatin subset revealed a strong enrichment of NF-κB-related signaling modules (**Figure 5F**). We selected CCL2, the gene with the highest weighted regulatory score, for further investigation. ChIP analysis demonstrated that the binding of p65 to the CCL2 promoter and enhancer were both significantly reduced in ATF2-deficient cells. ATAC-seq further indicated that this impaired binding may result from increased chromatin compaction at the CCL2 promoter and enhancer following ATF2 knockdown (**Figure 5G**). Consistently, GRO-seq analysis revealed a pronounced decrease in both sense and antisense

nascent transcripts of CCL2 after ATF2 depletion (**Figure 5H**). Interestingly, altering ATF2 levels through knockdown or overexpression did not affect p65 mRNA abundance, while the expression of multiple p65 downstream targets changed accordingly (**Figure 5I**, Figure S4D-E). This suggests that ATF2 does not regulate NF-κB signaling by controlling p65 transcription. Instead, IP-re-IP assays confirmed that ATF2 physically interacts with key NF-κB pathway components, including p65, and forms an ATF2-KAT3A-p65 complex that participates in chromatin remodeling (**Figure 5J**). Together, these results demonstrate that ATF2 is a critical regulator of enhancer activity at NF-κB-responsive regulatory elements.

ATF2 regulates CCL2 expression through dual mechanisms of enhancer accessibility and transcriptional activation

To further validate the role of ATF2-p65 cooperation in regulating p65 transcriptional activity, we performed ChIP-seq under ATF2-knockdown conditions. The results showed that p65 DNA-binding abundance was markedly reduced in ATF2-deficient cells, with significantly diminished enrichment at the promoters of key downstream targets, including IL-6, CD54, and CCL2 (**Figure 6A-B**). Consistently, ChIP-qPCR validation in Huh-7 cells demonstrated that for CCL2, knockdown of either p65 or ATF2 resulted in a substantial reduction of p65 occupancy at its promoter (**Figure 6C**). We next assessed the total RNA levels, nascent transcription, and enhancer RNA (eRNA) output of these downstream genes following ATF2 knockdown. In agreement with the ChIP results, CCL2 exhibited the most pronounced reduction across all transcriptional readouts. Interestingly, although knockdown of ATF2 led to a pronounced reduction in the total RNA and nascent RNA levels of IL-6, CD54, and CCL2, knockdown of p65 resulted in a much weaker decrease in CCL2 transcripts compared with IL-6 and CD54 (**Figure 6D-F**, Figure S5A-C). This observation suggests that ATF2 regulates CCL2 not solely through its enhancer-mediated facilitation of p65 activity, but also through additional p65-independent mechanisms.

Given that ATF2 possesses intrinsic transcription factor activity, we investigated whether ATF2 directly regulates CCL2 transcription. Both luciferase reporter assays and ChIP-PCR demonstrated that ATF2 can directly bind to and activate the CCL2 promoter WT2 (**Figure 6G-J**, Figure S5D-E). ChIP-qPCR results further demonstrated that ATF2 can also promote p65 enrichment at the CCL2 promoter by regulating H3K18la, thereby cooperatively enhancing p65-dependent transcription of CCL2 (**Figure 6K-L**, Figure S5F-G). Taken together, these results establish that ATF2 exerts a dual regulatory role over CCL2 expression-functioning both as an epigenetic organizer that modulates chromatin accessibility and as a transcription factor that directly drives CCL2 transcription.

Targeting ATF2 improves the efficacy of αPD-1 therapy in preclinical HCC models

To evaluate whether pharmacological inhibition of ATF2 enhances the antitumor efficacy of αPD-1 therapy, we established an orthotopic TIBx liver cancer model and administered the ATF2 inhibitor SBI-0087702 alone or in combination with αPD-1 (**Figure 7A**). Tumor burden analysis demonstrated that combined treatment produced the most pronounced antitumor effect, resulting in a significant reduction in tumor weight compared with either monotherapy (**Figure 7B**). Flow cytometric profiling of tumor-infiltrating immune cells revealed a marked decrease in $CD206^+$ M2-like macrophages with an increase in $CD86^+$ M1-like macrophages following ATF2 inhibition, an effect that was further amplified when SBI-0087702 was combined with αPD-1 (**Figure 7C**, Figure S6A). In parallel, the proportion of $CD8^+$ T cells was significantly increased in the combination group relative to the control and monotherapy groups (**Figure 7D**). Functional assessment of intratumoral $CD8^+$ T cells showed elevated expression of IFN-γ and GZMB and decreased expression of exhaustion markers PD-1 and LAG-3, indicating enhanced cytotoxic activation following ATF2 inhibition, with the strongest activation again observed in the combination group (**Figure 7E**). Immunofluorescence staining corroborated these

findings, revealing a substantial increase in $CD8^+$ T-cell infiltration and a marked reduction in $CD206^+$ macrophages within tumors treated with the combination therapy (**Figure 7F**). Importantly, overall survival analysis demonstrated that mice receiving the combined SBI-0087702 and αPD-1 treatment exhibited the most significant survival benefit, with markedly prolonged survival compared with all other groups (**Figure 7G**). Serum biochemical parameters, including AST, ALT, and ALB, remained within a comparable or improved range relative to controls, and no significant alterations were observed in renal or metabolic indicators (Figure S6D). Consistently, histopathological examination of major organs, including heart, spleen, lung, brain, and kidney, revealed no detectable tissue injury across treatment groups (Figure S6E). Together, these results indicate that ATF2 inhibition reshapes the tumor immune microenvironment by suppressing immunosuppressive M2 macrophages and enhancing $CD8^+$ T-cell effector function, thereby overcoming resistance to αPD-1 immunotherapy in liver cancer.

ATF2-H3K18la axis correlates with anti-PD-1 resistance in HCC

To examine whether ATF2-associated H3K18 lactylation is related to anti-PD-1 response in HCC, we performed immunohistochemical staining of tumor specimens from responders and non-responders. Representative images showed stronger ATF2 and H3K18la staining in non-responders than in responders (**Figure 8A**), and H-score quantification confirmed significantly higher levels of both markers in non-responders (**Figure 8B**). In parallel, the NF-κB-related inflammatory and chemokine targets CCL2, IL-6, and CD54 were markedly upregulated in non-responders, as shown by representative staining and quantitative analysis (**Figure 8C**).

We further assessed immune cell infiltration in these tumors. Non-responders exhibited increased $CD206^+$ macrophage density and reduced $CD8^+$ T-cell infiltration compared with responders (**Figure 8D**). Correlation analyses showed that ATF2 H-score positively correlated with H3K18la, CCL2, CD54, IL-6, and $CD206^+$ cell

density, but negatively correlated with $CD8^+$ cell density (**Figure 8E-J**). These data suggest that elevated ATF2-associated H3K18 lactylation is linked to NF-κB inflammatory/chemokine activation and an immunosuppressive tumor microenvironment in anti-PD-1 non-responding HCC.

Discussion

In this study, we identified ATF2 as a critical transcriptional and epigenetic regulator driving M2 macrophage polarization, immune evasion, and anti-PD-1 resistance in HCC. By integrating multi-omics analyses, functional experiments, preclinical therapeutic models, and clinical specimen validation, we demonstrated that ATF2 promotes an immunosuppressive TME through CCL2-dependent macrophage recruitment and KAT3A-mediated H3K18 lactylation, ultimately impairing cytotoxic $CD8^+$ T-cell function. Importantly, tumor specimens from anti-PD-1 non-responding HCC patients displayed elevated ATF2 and H3K18la levels, increased NF-κB-related inflammatory and chemokine markers, enhanced $CD206^+$ macrophage infiltration, and reduced $CD8^+$ T-cell abundance. These clinical associations support the relevance of the ATF2-H3K18la-NF-κB chemokine axis in human anti-PD-1 resistance. Pharmacologic inhibition of ATF2 markedly improved the efficacy of anti-PD-1 therapy, providing a potential combinatorial strategy to overcome immune resistance in HCC.

Our findings expand the current understanding of the transcriptional networks and epigenetic programs that shape macrophage behavior within the HCC TME. Previous studies have established that tumor-intrinsic pathways such as PKCα/ZFP64/CSF1 [34], RNase1/ALK [19], and SRSF10 [28] promote macrophage M2 polarization and confer resistance to PD-1 blockade. Our study adds to this framework by revealing ATF2 as a novel upstream transcriptional node that coordinates both chromatin remodeling and cytokine signaling to sustain M2 macrophage dominance. Notably, ATF2-mediated regulation of H3K18 lactylation through KAT3A represents an unrecognized mechanism by which metabolic-epigenetic crosstalk reinforces

tumor-promoting immunity.

Mechanistically, we identify a dual epigenetic and transcriptional program through which ATF2 orchestrates macrophage recruitment and polarization. ATF2 cooperates with KAT3A to enhance H3K18la deposition, maintaining open chromatin at NF-κB-responsive enhancers. This preserves enhancer accessibility for p65 binding, facilitating transcription of immunosuppressive genes such as CCL2. ATF2 also directly binds to the CCL2 promoter, acting as a transcription factor that drives CCL2 expression and macrophage recruitment. This dual mechanism underscores the multifaceted role of ATF2 in shaping the immunosuppressive landscape of HCC. Similar transcription factor-driven enhancer remodeling has been implicated in the function of c-Maf, another macrophage-regulatory factor that promotes M2 polarization and αPD-1 resistance in lung cancer [35]. Our study provides the first evidence that ATF2 exerts analogous immunoregulatory control in liver cancer through epigenetic coupling with histone lactylation machinery.

Importantly, CCL2 should be interpreted as a mechanistically and functionally validated effector rather than the sole transcriptional output of ATF2 activity. Our integrated RNA-seq, ATAC-seq, ChIP-seq, and GRO-seq analyses indicate that ATF2 broadly licenses NF-κB-responsive regulatory elements through KAT3A-dependent H3K18 lactylation. CCL2 was selected for in-depth validation because it showed prominent transcriptional dependence on ATF2 and because perturbation and rescue experiments established its functional requirement for macrophage recruitment and immunosuppressive polarization. Thus, the ATF2-KAT3A-H3K18la axis should be viewed as an upstream epigenetic mechanism that coordinates a broader chemokine and inflammatory program, with CCL2 representing a dominant macrophage-directed arm.

Within this broader ATF2-dependent chemokine program, the identification of CCL2 as a dominant macrophage-directed effector is consistent with prior evidence that CCL2-CCR2 signaling drives immunosuppressive TAM infiltration and suppresses antitumor immunity [36]. Moreover, our data demonstrate that ATF2 activity not only

amplifies CCL2 transcription but also enhances NF-κB-dependent activation, revealing a feed-forward circuit between ATF2 and p65 that sustains chronic inflammation and immunosuppression within the TME. This mechanism parallels other immune escape pathways in HCC, such as the MVP-STAT6 axis, which also reinforces M2 polarization through transcriptional cooperation [37].

Beyond immune modulation, our findings link ATF2 to histone lactylation, a recently identified epigenetic mark that integrates cellular metabolism with gene expression [27]. ATF2-high tumors display markedly elevated global lactylation and, in particular, increased H3K18la, a modification enriched in metabolically reprogrammed tumor microenvironments [38-40]. Although ATF2 does not directly recognize lactylated histones, it physically engages the acetyltransferase KAT3A, which we identify as a key writer of H3K18la in HCC [41]. Elevated H3K18la levels in αPD-1 resistant HCC and their dependency on ATF2-KAT3A interaction highlight a potential intersection between metabolic adaptation and epigenetic reprogramming in shaping immune tolerance. Consistently, our clinical IHC analysis showed that H3K18la was elevated in anti-PD-1 non-responders and positively correlated with ATF2 expression, further supporting the clinical relevance of this epigenetic axis in immunotherapy-resistant HCC. Given that lactate accumulation within the TME is a hallmark of HCC metabolic reprogramming, ATF2 may act as a sensor that translates tumor-derived metabolic cues into immune regulatory transcriptional programs.

Therapeutically, targeting this network yields substantial benefit. Pharmacologic inhibition of ATF2 not only reduces tumor burden and TAM infiltration but also enhances $CD8^+$ T-cell infiltration and effector cytokine production. Notably, ATF2 inhibition synergizes with PD-1 blockade, converting resistant tumors into responders and prolonging survival without overt toxicity. These results complement emerging evidence that epigenetic regulators dictating enhancer dynamics, such as KAT3A, BRD4, and SWI/SNF components, serve as master determinants of immunotherapy responsiveness [42, 43]. By positioning ATF2 upstream of both CCL2-driven macrophage recruitment and KAT3A-dependent enhancer activation, our study

reveals a therapeutically actionable node whose modulation can reprogram the tumor immune microenvironment.

In summary, our findings uncover ATF2 as a central orchestrator of immunosuppressive remodeling in HCC, integrating metabolic epigenetics, cytokine signaling, and enhancer regulation to support M2 macrophage recruitment and sustain PD-1 resistance. Targeting ATF2 disrupts this multilayered network and restores anti-tumor immunity, providing a mechanistic rationale for ATF2 inhibition as a strategy to overcome immune checkpoint resistance in HCC (**Schematic**).

Methods

Patients and samples

A total of 91 tumor specimens from HCC patients who underwent surgical resection at Huashan Hospital, Fudan University were collected for immunohistochemistry (IHC) analyses. In addition, pretreatment liver biopsy samples from another 62 HCC patients receiving αPD-1 therapy were analyzed by IHC. Tumor response was evaluated based on the modified Response Evaluation Criteria in Solid Tumors (mRECIST) [44], and patient classification into responders and non-responders followed established criteria [26]. The 91 resected HCC specimens were used for ATF2 IHC analysis and clinicopathological correlation. The 62 pretreatment biopsy specimens from patients receiving αPD-1 therapy were used for IHC or multiplex IF comparison between responders and non-responders. For bulk RNA-seq, samples were stratified into M2Φhigh and M2Φlow groups according to flow cytometry. The study was reviewed and approved by the Research Ethics Committees of Fudan University (2021-856), with written informed consent obtained from all participants, in accordance with the principles of the Declaration of Helsinki.

Cell lines and cell culture

Huh-7 (Cat# CTCC-003-0019), SNU-475 (Cat# CTCC-007-0149), SNU-387 (Cat# CTCC-400-0147), and JHH-4 (Cat# CTCC-001-0806) cells were purchased from Meisen China Tissue Culture Bank. TIBx cells were obtained from ATCC (Cat# CRL-3641). Hepa 53.4 cells were purchased from Wuhan Warner Biotechnology Co., Ltd. (Cat# WN-105307). Huh-7, JHH-4, TIBx, and Hepa 53.4 cells were cultured in Dulbecco's modified Eagle's medium (DMEM; Gibco, Cat# 11965092), while SNU-475 and SNU-387 cells were maintained in RPMI 1640 medium (Gibco, Cat# 11875093). All culture media were supplemented with 10% fetal bovine serum (FBS; Gibco, Cat# 10099141C) and 1% penicillin-streptomycin solution (Gibco, Cat# 15140122). Cells were maintained at 37°C in a humidified incubator with 5% CO_2 and passaged every 3-5 days according to their growth rate using 0.25% trypsin-EDTA (Gibco, Cat# 25200056).

Mice and animal experiments

Specific pathogen-free (SPF) C57BL/6J mice and BALB/c mice were purchased from GemPharmatech Co., Ltd. (Jiangsu, China). Male mice aged 6-8 weeks and weighing 18-22 g were used for all animal experiments unless otherwise indicated. Mice were maintained in an SPF-grade animal facility under controlled conditions with a 12h light/12h dark cycle, temperature of 22 ± 2°C, and relative humidity of 50-60%. Animals were housed in individually ventilated cages with autoclaved bedding and were provided with sterile water and standard rodent chow ad libitum. Mice were acclimatized for at least 1 week before experimental manipulation.

All animal procedures were approved by the Institutional Animal Care and Use Committee of Fudan University (202311014S), and were performed in accordance with institutional guidelines for animal welfare. Mice were randomly assigned to experimental groups, and investigators were blinded to group allocation during tumor measurement, flow cytometric analysis, histological assessment, and survival evaluation whenever feasible. No fasting was performed before experimental

procedures, and all interventions were carried out during the light phase. For surgical procedures, mice were anesthetized with isoflurane (RWD Life Science, Cat# R510-22) using an animal anesthesia system. Humane endpoints were predefined, and mice were euthanized when tumor burden exceeded ethical limits, body weight loss exceeded 20%, or severe distress, impaired mobility, ulceration, or moribund status was observed. Euthanasia was performed by CO_2 inhalation followed by cervical dislocation.

Orthotopic liver tumor model

Orthotopic HCC was established by intrahepatic injection of syngeneic tumor cells as previously described [45]. Briefly, mice were anesthetized with 2% isoflurane, and the abdomen was disinfected with povidone-iodine and 75% ethanol. A small left subcostal incision was made to expose the left liver lobe. A total of 1×10^6 tumor cells suspended in 20 μL of a 1:1 mixture of sterile PBS and growth factor-reduced Matrigel Matrix (Corning, Cat# 356231) were slowly injected into the subcapsular region of the left liver lobe using a 29-gauge insulin syringe. After injection, gentle compression was applied with a sterile cotton swab for 1-2 min to prevent leakage and bleeding. The liver was then returned to the abdominal cavity, and the peritoneum and skin were closed using absorbable sutures.

For ATF2 loss-of-function experiments, control or ATF2-knockout TIBx cells were orthotopically implanted into syngeneic mice. For ATF2 gain-of-function experiments, control or ATF2-overexpressing Hepa 53.4 cells were implanted using the same procedure. Tumor-bearing mice were monitored every 2-3 days and sacrificed at the indicated time points for tumor burden assessment, flow cytometry, histology, immunofluorescence, and molecular analyses.

M2 macrophage adoptive transfer

For M2 macrophage adoptive transfer experiments, bone marrow-derived macrophages (BMDMs) were generated from femurs and tibias of naïve BALB/c mice. Bone marrow cells were cultured in RPMI 1640 medium supplemented with 10% FBS, 1% penicillin-streptomycin, and recombinant murine M-CSF (PeproTech, Cat# 315-02) at 20 ng/mL for 7 days to induce macrophage differentiation. To obtain M2-polarized macrophages, mature BMDMs were further stimulated with recombinant murine IL-4 (PeproTech, Cat# 214-14) and IL-13 (PeproTech, Cat# 210-13) at 20 ng/mL each for 24h. M2 polarization was confirmed by flow cytometry and/or RT-qPCR based on the expression of CD206, Arg1, Il10, and Tgfb1.

For adoptive transfer, M2-polarized macrophages were harvested, washed twice with sterile PBS, and resuspended at 5×10^6 cells/mL. Tumor-bearing mice received 1×10^6 M2 macrophages in 200 μL sterile PBS via tail vein injection every 4 days after tumor implantation. Control mice received an equal volume of sterile PBS. Tumors were harvested at the indicated endpoints for analysis of tumor growth, macrophage infiltration, macrophage polarization, and $CD8^+$ T-cell function.

Macrophage differentiation and co-culture

Human THP-1 monocytes were obtained from ATCC (Cat# TIB-202) and maintained in RPMI 1640 medium (Gibco, Cat# 11875093) supplemented with 10% fetal bovine serum (FBS; Gibco, Cat# 10099141C) and 1% penicillin-streptomycin solution (Gibco, Cat# 15140122) at 37°C in a humidified incubator containing 5% CO_2. THP-1 cells were differentiated into macrophage-like cells by treatment with 100 nM phorbol 12-myristate 13-acetate (PMA; Sigma-Aldrich, Cat# P1585) for 48 h. PMA was dissolved in dimethyl sulfoxide (DMSO; Sigma-Aldrich, Cat# D2650), and an equal volume of DMSO was used as the vehicle control. After PMA stimulation, cells were washed twice with sterile PBS (Gibco, Cat# 10010023) and rested in fresh complete RPMI 1640 medium for 24 h before co-culture.

For non-contact co-culture assays, differentiated THP-1-derived macrophages and

HCC cells were co-cultured using 24-well Transwell inserts with 0.4 μm pore polycarbonate membranes (Corning, Cat# 3413), which allow the exchange of soluble factors while preventing direct cell-cell contact. HCC cells were seeded in the lower chamber, and THP-1-derived macrophages were seeded in the upper insert at a macrophage:HCC cell ratio of 1:3. Co-cultures were maintained in complete medium for 72 h. Macrophages were then harvested for RT-qPCR, flow cytometry, or other downstream analyses.

Statistical analysis

All experiments were performed with at least three independent biological replicates unless otherwise stated. For animal experiments, the number of mice per group is indicated in the corresponding figure legends. Data are presented as mean ± standard error of the mean (SEM). Statistical analyses were performed using GraphPad Prism 9.0 and R software where appropriate. For comparisons between two groups, an unpaired two-tailed Student's t-test was used for normally distributed data. For comparisons among more than two groups, one-way ANOVA followed by Tukey's multiple-comparisons test was applied. For experiments involving two independent variables, two-way ANOVA followed by Tukey's multiple-comparisons test was used. Survival curves were generated using the Kaplan-Meier method and compared using the log-rank Mantel-Cox test. Correlation analyses between gene expression levels and immune cell infiltration scores or marker gene expression were performed using Spearman's correlation test. P value < 0.05 was considered statistically significant. Statistical significance was denoted as follows: *P < 0.05, **P < 0.01, and ***P < 0.001.

References

1. El-Khoueiry, A.B., et al., *Nivolumab in patients with advanced hepatocellular carcinoma (CheckMate 040): an open-label, non-comparative, phase 1/2 dose*

escalation and expansion trial. Lancet (London, England), 2017. **389**(10088): p. 2492-2502.

2. Finn, R.S., et al., *Atezolizumab plus Bevacizumab in Unresectable Hepatocellular Carcinoma.* The New England Journal of Medicine, 2020. **382**(20): p. 1894-1905.
3. Kole, C., et al., *Immunotherapy for Hepatocellular Carcinoma: A 2021 Update.* Cancers, 2020. **12**(10).
4. Hao, L., et al., *The current status and future of targeted-immune combination for hepatocellular carcinoma.* Frontiers In Immunology, 2024. **15**: p. 1418965.
5. Myojin, Y., et al., *Multiomics analysis of immune correlatives in hepatocellular carcinoma patients treated with tremelimumab plus durvalumab.* Gut, 2025. **74**(6): p. 983-995.
6. Wang, Z., et al., *Immune checkpoint inhibitor resistance in hepatocellular carcinoma.* Cancer Letters, 2022. **555**: p. 216038.
7. Tang, T., et al., *Advantages of targeting the tumor immune microenvironment over blocking immune checkpoint in cancer immunotherapy.* Signal Transduction and Targeted Therapy, 2021. **6**(1): p. 72.
8. Chen, S., et al., *Macrophages in immunoregulation and therapeutics.* Signal Transduction and Targeted Therapy, 2023. **8**(1): p. 207.
9. Cheng, K., et al., *Tumor-associated macrophages in liver cancer: From mechanisms to therapy.* Cancer Communications (London, England), 2022. **42**(11): p. 1112-1140.
10. Jia, W., et al., *Hypoxia-induced RCOR2 promotes macrophage M2 polarization and CD8+ T-cell exhaustion by enhancing LIF transcription in hepatocellular carcinoma.* Journal For Immunotherapy of Cancer, 2025. **13**(10).
11. Liu, Y., et al., *Identification of a tumour immune barrier in the HCC microenvironment that determines the efficacy of immunotherapy.* Journal of Hepatology, 2023. **78**(4): p. 770-782.
12. Feng, Q., H. Lu, and L. Wu, *Identification of M2-like macrophage-related*

signature for predicting the prognosis, ecosystem and immunotherapy response in hepatocellular carcinoma. PloS One, 2023. **18**(9): p. e0291645.

13. Mi, H., et al., *Multi-Scale Spatial Analysis of the Tumor Microenvironment Reveals Features of Cabozantinib and Nivolumab Efficacy in Hepatocellular Carcinoma.* Frontiers In Immunology, 2022. **13**: p. 892250.
14. Weng, J., et al., *Intratumoral PPT1-positive macrophages determine immunosuppressive contexture and immunotherapy response in hepatocellular carcinoma.* Journal For Immunotherapy of Cancer, 2023. **11**(6).
15. Li, X., et al., *Integrated Single Cell Analysis Reveals An Atlas of Tumor Associated Macrophages in Hepatocellular Carcinoma.* Inflammation, 2024. **47**(6): p. 2077-2093.
16. Le, J., et al., *Single-cell multi-omics in cancer immunotherapy: from tumor heterogeneity to personalized precision treatment.* Molecular Cancer, 2025. **24**(1): p. 221.
17. Lei, K., et al., *Integrative multi-omics and Mendelian randomization analysis reveal SPP1+ tumor-associated macrophage-driven prognostic signature for hepatocellular carcinoma.* Frontiers In Molecular Biosciences, 2025. **12**: p. 1594610.
18. Shiau, D.-J., et al., *Hepatocellular carcinoma-derived high mobility group box 1 triggers M2 macrophage polarization via a TLR2/NOX2/autophagy axis.* Scientific Reports, 2020. **10**(1): p. 13582.
19. Liu, C., et al., *Targeting ALK averts ribonuclease 1-induced immunosuppression and enhances antitumor immunity in hepatocellular carcinoma.* Nature Communications, 2024. **15**(1): p. 1009.
20. Watson, G., Z.e.A. Ronai, and E. Lau, *ATF2, a paradigm of the multifaceted regulation of transcription factors in biology and disease.* Pharmacological Research, 2017. **119**: p. 347-357.
21. Chen, M., et al., *Emerging roles of activating transcription factor (ATF) family members in tumourigenesis and immunity: Implications in cancer immunotherapy.* Genes & Diseases, 2021. **9**(4): p. 981-999.

22. Duyndam, M.C., et al., *The N-terminal transactivation domain of ATF2 is a target for the co-operative activation of the c-jun promoter by p300 and 12S E1A.* Oncogene, 1999. **18**(14): p. 2311-2321.
23. Bruhat, A., et al., *ATF2 is required for amino acid-regulated transcription by orchestrating specific histone acetylation.* Nucleic Acids Research, 2007. **35**(4): p. 1312-1321.
24. Li, L., et al., *TOP2A, Stabilized by IGF2BP3 in an m6A-Dependent Manner, Drives Macrophage Recruitment and M2 Polarization in Hepatocellular Carcinoma by YAP1-Mediated CCL2 Activation.* Molecular Carcinogenesis, 2025.
25. Flores-Toro, J.A., et al., *CCR2 inhibition reduces tumor myeloid cells and unmasks a checkpoint inhibitor effect to slow progression of resistant murine gliomas.* Proceedings of the National Academy of Sciences of the United States of America, 2019. **117**(2): p. 1129-1138.
26. Zhou, C., et al., *Disruption of SLFN11 Deficiency-Induced CCL2 Signaling and Macrophage M2 Polarization Potentiates Anti-PD-1 Therapy Efficacy in Hepatocellular Carcinoma.* Gastroenterology, 2023. **164**(7): p. 1261-1278.
27. Yu, X., et al., *Histone lactylation: from tumor lactate metabolism to epigenetic regulation.* International Journal of Biological Sciences, 2024. **20**(5): p. 1833-1854.
28. Cai, J., et al., *Targeting SRSF10 might inhibit M2 macrophage polarization and potentiate anti-PD-1 therapy in hepatocellular carcinoma.* Cancer Communications (London, England), 2024. **44**(11): p. 1231-1260.
29. Zhang, D., et al., *Metabolic regulation of gene expression by histone lactylation.* Nature, 2019. **574**(7779): p. 575-580.
30. Lv, M., et al., *Lactylation modification in cancer: mechanisms, functions, and therapeutic strategies.* Experimental Hematology & Oncology, 2025. **14**(1): p. 32.
31. Zabransky, D.J., et al., *Profiling of syngeneic mouse HCC tumor models as a framework to understand anti-PD-1 sensitive tumor microenvironments.*

Hepatology (Baltimore, Md.), 2023. **77**(5): p. 1566-1579.

32. Li, X., et al., *Targeting of tumour-infiltrating macrophages via CCL2/CCR2 signalling as a therapeutic strategy against hepatocellular carcinoma.* Gut, 2015. **66**(1): p. 157-167.

33. Weng, J., et al., *Repolarization of Immunosuppressive Macrophages by Targeting SLAMF7-Regulated CCL2 Signaling Sensitizes Hepatocellular Carcinoma to Immunotherapy.* Cancer Research, 2024. **84**(11): p. 1817-1833.

34. Wei, C.-Y., et al., *PKCα/ZFP64/CSF1 axis resets the tumor microenvironment and fuels anti-PD1 resistance in hepatocellular carcinoma.* Journal of Hepatology, 2022. **77**(1): p. 163-176.

35. Liu, M., et al., *Transcription factor c-Maf is a checkpoint that programs macrophages in lung cancer.* The Journal of Clinical Investigation, 2020. **130**(4): p. 2081-2096.

36. Wang, Y., et al., *mRNA Delivery of a Bispecific Single-Domain Antibody to Polarize Tumor-Associated Macrophages and Synergize Immunotherapy against Liver Malignancies.* Advanced Materials (Deerfield Beach, Fla.), 2021. **33**(23): p. e2007603.

37. Yu, C., et al., *Major vault protein regulates tumor-associated macrophage polarization through interaction with signal transducer and activator of transcription 6.* Frontiers In Immunology, 2024. **14**: p. 1289795.

38. Zhang, C., et al., *H3K18 Lactylation Potentiates Immune Escape of Non-Small Cell Lung Cancer.* Cancer Research, 2024. **84**(21): p. 3589-3601.

39. Li, W., et al., *Tumor-derived lactate promotes resistance to bevacizumab treatment by facilitating autophagy enhancer protein RUBCNL expression through histone H3 lysine 18 lactylation (H3K18la) in colorectal cancer.* Autophagy, 2023. **20**(1): p. 114-130.

40. Li, F., et al., *Positive feedback regulation between glycolysis and histone lactylation drives oncogenesis in pancreatic ductal adenocarcinoma.* Molecular Cancer, 2024. **23**(1): p. 90.

41. Dong, M., et al., *ASF1A-dependent P300-mediated histone H3 lysine 18*

lactylation promotes atherosclerosis by regulating EndMT. Acta Pharmaceutica Sinica. B, 2024. **14**(7): p. 3027-3048.

42. Kikuchi, M., et al., *Epigenetic mechanisms to propagate histone acetylation by p300/CBP.* Nature Communications, 2023. **14**(1): p. 4103.

43. Zhu, H., et al., *BET Bromodomain Inhibition Promotes Anti-tumor Immunity by Suppressing PD-L1 Expression.* Cell Reports, 2016. **16**(11): p. 2829-2837.

44. Lencioni, R. and J.M. Llovet, *Modified RECIST (mRECIST) assessment for hepatocellular carcinoma.* Seminars In Liver Disease, 2010. **30**(1): p. 52-60.

45. Brown, Z.J., B. Heinrich, and T.F. Greten, *Establishment of Orthotopic Liver Tumors by Surgical Intrahepatic Tumor Injection in Mice with Underlying Non-Alcoholic Fatty Liver Disease.* Methods and Protocols, 2018. **1**(2).

Figure legends

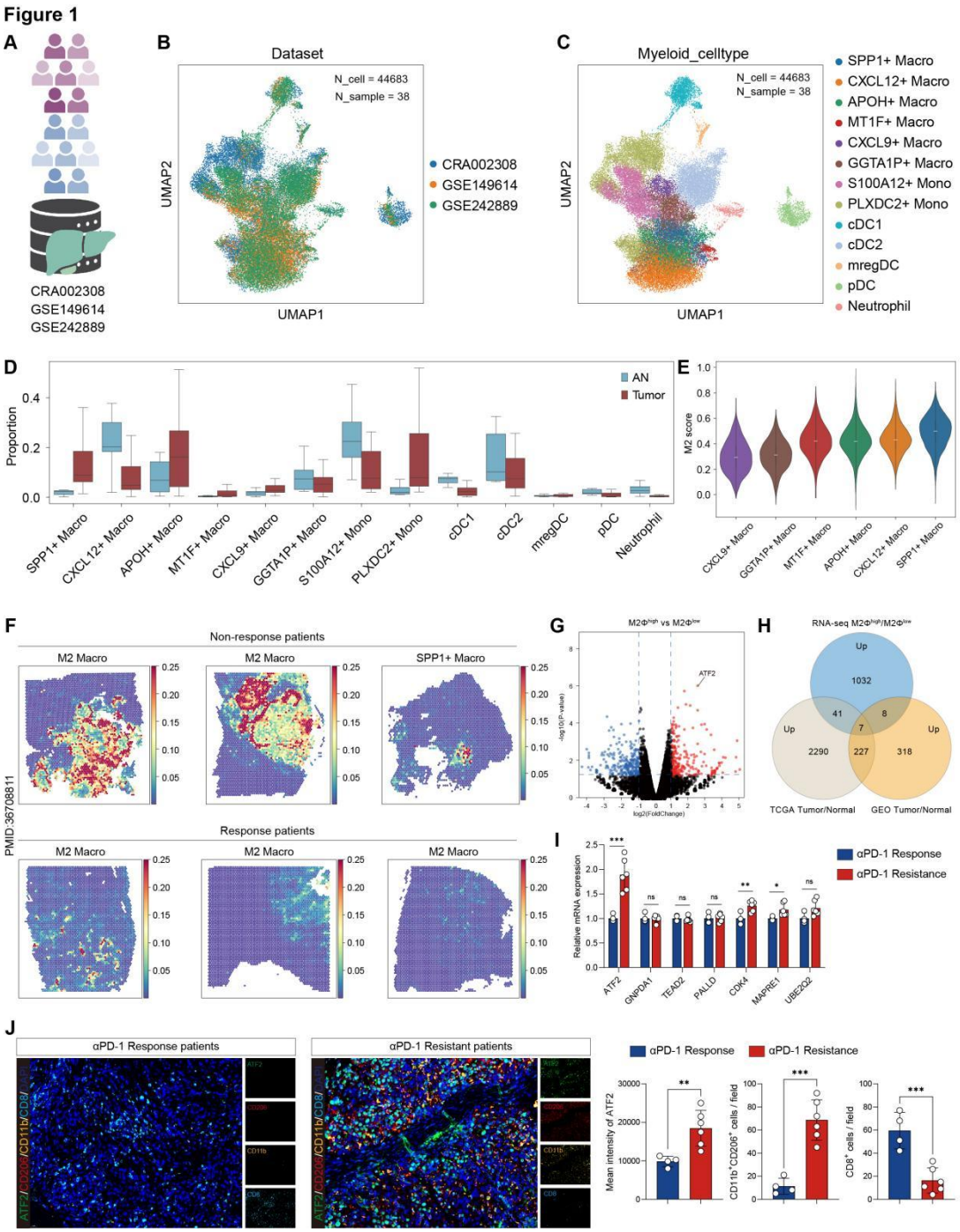


Figure 1. ATF2 is a key regulator associated with M2 macrophage enrichment and αPD-1 resistance in HCC. (**A**) Schematic overview of integrated scRNA-seq datasets from three public cohorts (CRA002308, GSE149614, and GSE242889). **(B)** Uniform Manifold Approximation and Projection (UMAP) visualization showing cell distributions across datasets. **(C)** UMAP plot illustrating the identification of 11 major

myeloid subtypes, including macrophage, monocyte, dendritic cell (DC), plasmacytoid DC (pDC), and neutrophil populations. **(D)** Proportion of myeloid subpopulations between adjacent normal (AN) and tumor tissues. **(E)** Violin plot showing increased M2 polarization and decreased M1 polarization scores in tumor-associated macrophages compared with adjacent tissues. (F) Spatial transcriptomic analysis of representative αPD-1-responsive and non-responsive patients showing the distribution of M2 macrophages, which were enriched in non-responders. (**G**) Volcano plot of DEGs between $M2\Phi^{high}$ and $M2\Phi^{low}$ HCC. **(H)** Venn diagram integrating DEGs from $M2\Phi^{high}$ versus $M2\Phi^{low}$ HCC, TCGA tumor versus normal, and GEO datasets. **(I)** RT-qPCR validation showing elevated ATF2 expression in αPD-1-resistant HCC samples. **(J)** Representative immunofluorescence staining of ATF2 (green), CD206 (red), CD11b (yellow) and CD8 (cyan) in αPD-1-responsive and resistant tumors (left panel). Quantification of ATF2 fluorescence intensity, $CD11b^{+}CD206^{+}$ macrophages, and $CD8^{+}$ T-cell density (right panel). Data are shown as mean ± SEM; Statistical significance was determined by two-tailed Student's t-test for two-group comparisons and one-way ANOVA followed by Tukey's multiple-comparisons test for comparisons among multiple groups. (*P < 0.05, **P < 0.01, ***P < 0.001).

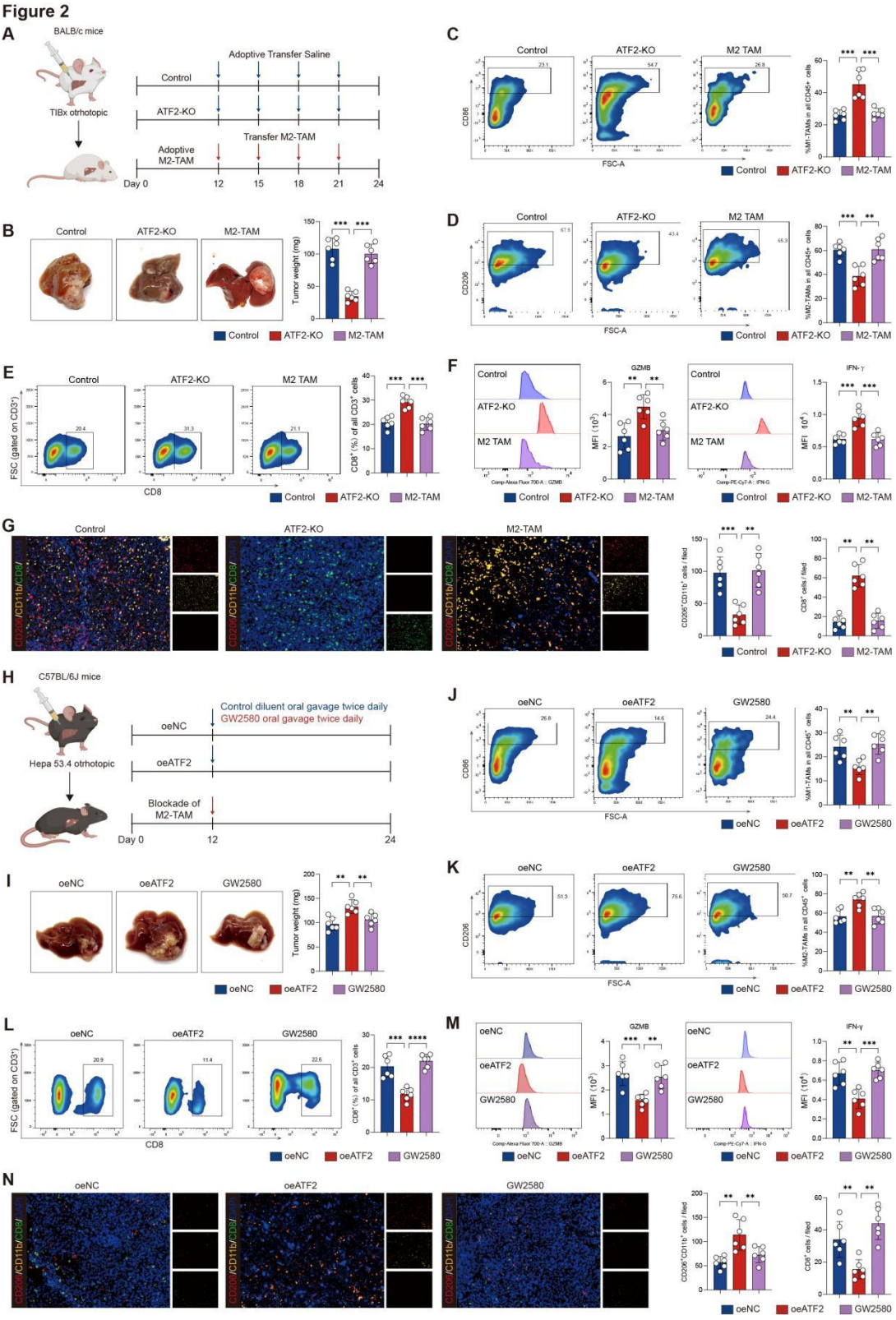


Figure 2. ATF2 promotes M2-like macrophage polarization and suppresses antitumor immunity in HCC. (A) Experimental design of the TIBx orthotopic HCC model in BALB/c mice. Tumor-bearing mice were divided into control, ATF2 knockout

(ATF2-KO), and M2 macrophage adoptive transfer (M2-TAM) groups to assess the effect of ATF2 deletion and M2 macrophage restoration on tumor progression. **(B)** Representative liver images and quantification of tumor weights showing that ATF2 knockout significantly reduced tumor growth, while adoptive transfer of M2 macrophages restored tumor burden. **(C-D)** Flow cytometric analysis of tumor-infiltrating macrophages. ATF2 knockout decreased the proportion of $CD206^+$ (M2-like) macrophages and increased $CD86^+$ (M1-like) macrophages, whereas adoptive transfer of M2 macrophages reversed these changes, restoring M2 dominance. **(E)** Representative flow cytometry plots showing infiltration of $CD8^+$ T cells among total $CD3^+$ lymphocytes. **(F)** Flow cytometric quantification of $CD8^+$ T-cell effector molecules GZMB and IFN-γ. **(G)** Representative multicolor immunofluorescence images of tumor tissues stained for CD206 (red), CD11b (yellow), and CD8 (green) with DAPI (blue). **(H)** Experimental scheme of the Hepa53.4 orthotopic HCC model used to assess the impact of ATF2 overexpression and M2 macrophage inhibition (GW2580 treatment). **(I)** Representative liver images and tumor weight quantification showing that ATF2 overexpression promoted tumor growth, while GW2580 treatment significantly reduced tumor burden. **(J-K)** Flow cytometric analysis demonstrating that ATF2 overexpression increased the proportion of $CD206^+$ M2 macrophages and decreased $CD86^+$ M1 macrophages. **(L)** Flow cytometric quantification of $CD8^+$ T-cell infiltration in tumors. **(M)** Flow cytometric analysis of $CD8^+$ T-cell effector function. ATF2 overexpression decreased GZMB and IFN-γ expression, indicative of T-cell exhaustion, while GW2580 treatment reactivated $CD8^+$ T-cell cytotoxic function. **(N)** Multicolor immunofluorescence images of tumor sections showing CD206 (red), CD11b (yellow), and CD8 (green) staining. Data are shown as mean ± SEM. Statistical significance was determined by two-tailed Student's t-test for two-group comparisons and one-way ANOVA followed by Tukey's multiple-comparisons test for comparisons among multiple groups (*$P < 0.05$, **$P < 0.01$, ***$P < 0.001$).

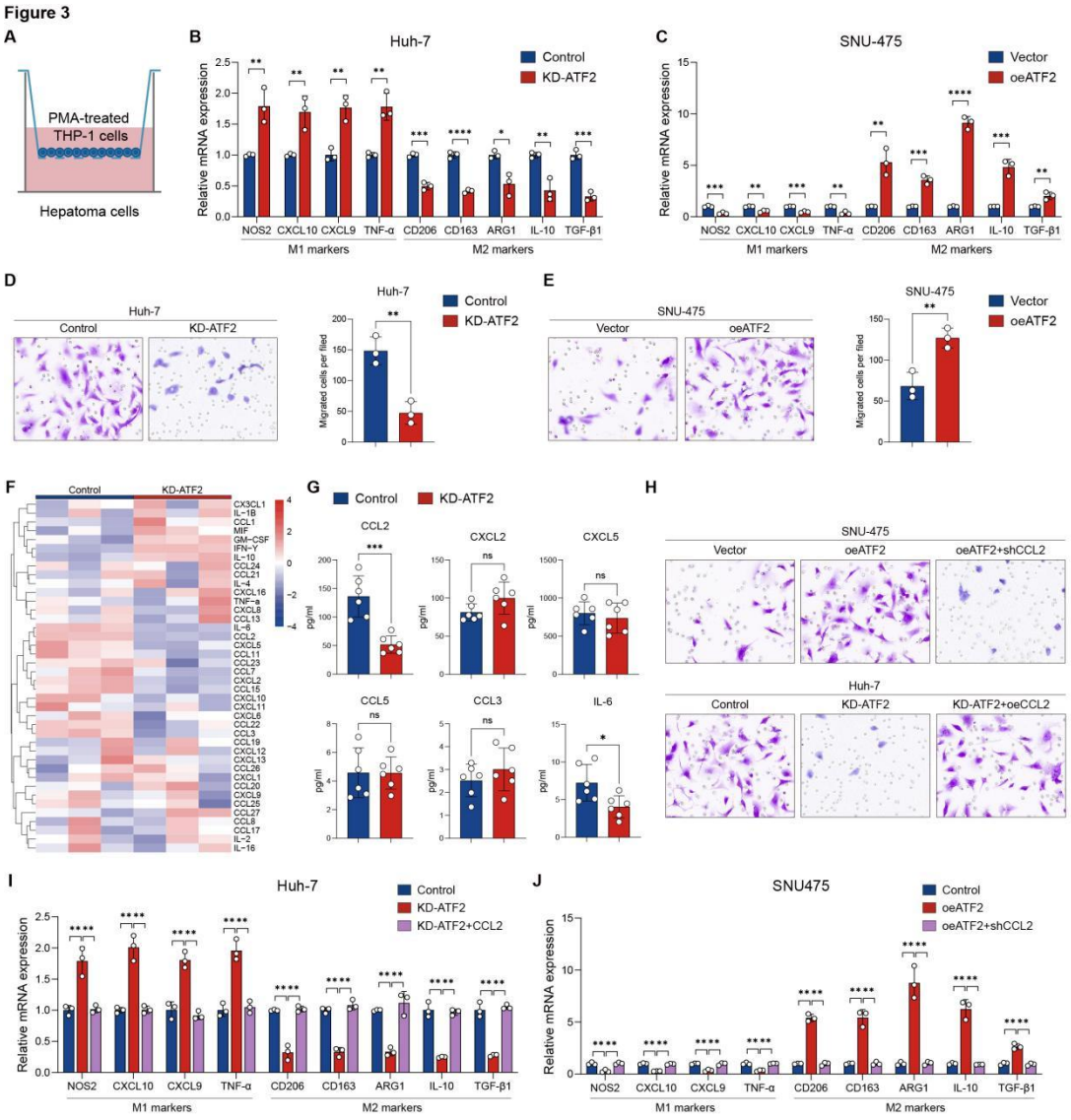


Figure 3. Tumor cell-intrinsic ATF2 regulates macrophage M2-like polarization and migration through a CCL2-dependent manner. (A) Schematic illustration of the *in vitro* co-culture system established using HCC cells and THP-1-derived macrophages to assess the role of tumor cell-intrinsic ATF2 in macrophage regulation. **(B-C)** RT-qPCR analysis showing the indicated M1-associated genes (NOS2, CXCL10, CXCL9, TNF-α) and M2-associated genes (CD206, CD163, ARG1, TGF-β1, IL-10) expression levels in THP-1-derived macrophages after co-culture with ATF2 knockdown or overexpressing HCC cells. **(D-E)** Chemotaxis assays showing the effect of supernatants from the indicated co-culture system on the migration ability of macrophage-differentiated THP-1 cells. **(F)** RT-qPCR screening results for downstream chemokines regulated by ATF2. **(G)** ELISA assays confirmed CCL2 is the

key downstream mediator for ATF2. **(H)** Chemotaxis assays showing the effect of supernatants from the indicated co-culture system on the migration ability of macrophage-differential THP-1 cells. **(I)** RT-qPCR analysis showing the indicated M1-associated genes (NOS2, CXCL10, CXCL9, TNF-α) and M2-associated genes (CD206, CD163, ARG1, TGF-β1, IL-10) expression levels in CCL2 overexpressing ATF2 knockdown Huh-7 cells. **(J)** RT-qPCR analysis showing the indicated M1-associated genes (NOS2, CXCL10, CXCL9, TNF-α) and M2-associated genes (CD206, CD163, ARG1, TGF-β1, IL-10) expression levels in CCL2 knockdown ATF2 overexpressing SNU475 cells. Data are shown as mean ± SEM; Statistical significance was determined by two-tailed Student's t-test for two-group comparisons and one-way ANOVA followed by Tukey's multiple-comparisons test for comparisons among multiple groups (*P < 0.05, **P < 0.01, ***P < 0.001).

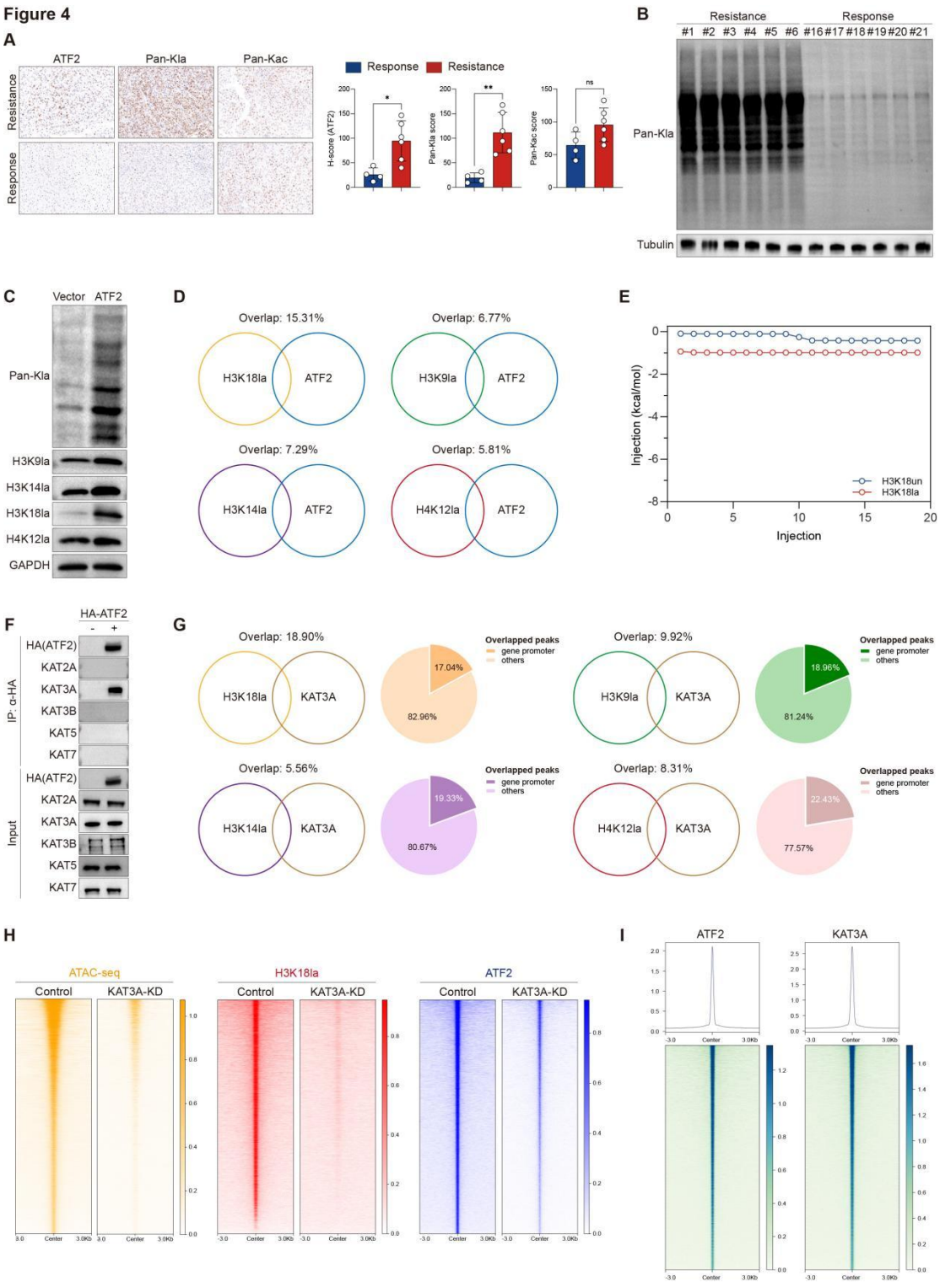


Figure 4. ATF2 cooperates with KAT3A to increase overall histone lactylation and selectively enrich H3K18la. (A) IHC results of ATF2, pan-lactylation (Pan-Kla), and Pan-Kac in human HCC samples stratified by response versus resistance to αPD-1 therapy. **(B)** Western blot analysis of pan-Kla in tumor tissues from αPD-1 resistant and responsive HCC patients. **(C)** Immunoblotting of lactylation markers in

ATF2-overexpressing SNU-475 cells. **(D)** Genome-wide overlap between ATF2 ChIP-seq peaks and lactylation marks (H3K18la, H3K9la, H3K14la, H4K12la). **(E)** Isothermal titration calorimetry (ITC) evaluating the binding between ATF2 and unmodified versus lactylated H3K18 peptides. **(F)** Co-immunoprecipitation demonstrating physical interaction between ATF2 and KAT3A, but not other histone lactylation writers. **(G)** Overlap analysis of KAT3A ChIP-seq peaks with lactylation marks (H3K18la, H3K9la, H3K14la, H4K12la). **(H)** Heatmaps from ATAC-seq, H3K18la ChIP-seq, and ATF2 ChIP-seq showing that KAT3A knockdown markedly reduces chromatin accessibility. **(I)** Average density plots and heatmaps illustrating the ATF2 and KAT3A enrichment at genomic loci. Data are shown as mean ± SEM. Statistical significance was determined by two-tailed Student's t-test for two-group comparisons and one-way ANOVA followed by Tukey's multiple-comparisons test for comparisons among multiple groups (*P < 0.05, **P < 0.01, ***P < 0.001).

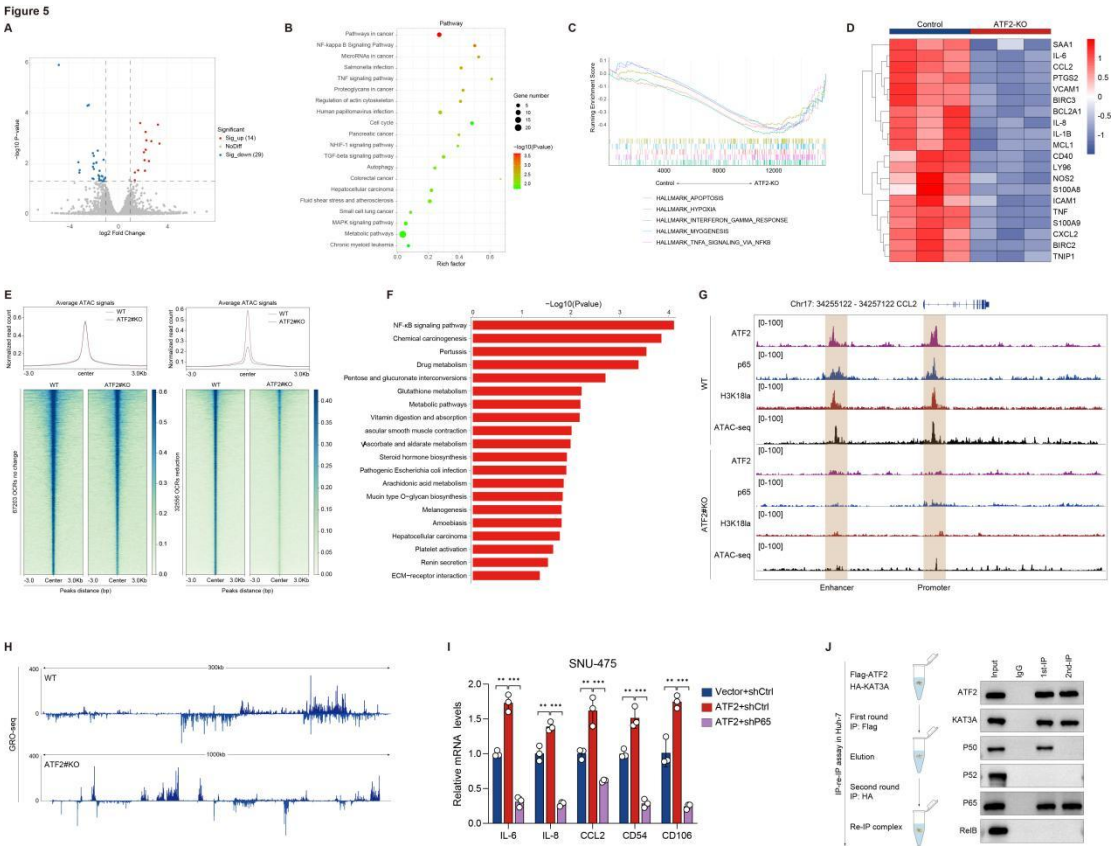


Figure 5. ATF2 maintains enhancer accessibility to support NF-κB–dependent transcription. (A) Volcano plot showing differentially expressed genes (DEGs) in ATF2-knockout HCC cells compared with controls. **(B)** KEGG pathway enrichment of ATF2-dependent DEGs highlighting significant enrichment of inflammatory and NF-κB-related signaling pathways. **(C)** GSEA demonstrating reduced activation of multiple NF-κB-associated pathways upon ATF2 depletion. **(D)** Heatmap of selected NF-κB downstream target genes transcriptional suppression in in ATF2-KO cells. **(E)** ATAC-seq metagene plots and heatmaps illustrating a marked reduction in chromatin accessibility following ATF2 knockdown. **(F)** Functional enrichment of promoter-proximal peaks that closed upon ATF2 loss, demonstrating strong enrichment for NF-κB-related regulatory modules. **(G)** Integrative ChIP-seq and ATAC-seq tracks at the CCL2 locus. **(H)** GRO-seq analysis showing substantial reduction in both sense and antisense nascent transcription of CCL2 in ATF2-KO cells. **(I)** RT-qPCR validation confirming selective downregulation of NF-κB target genes in SNU-475. **(J)** IP-re-IP assays revealing that p65 physically associates with ATF2 and KAT3A. Data are shown as mean ± SEM; Statistical significance was determined by two-tailed Student's t-test for two-group comparisons and one-way ANOVA followed by Tukey's multiple-comparisons test for comparisons among multiple groups (*P < 0.05, **P < 0.01, ***P < 0.001).

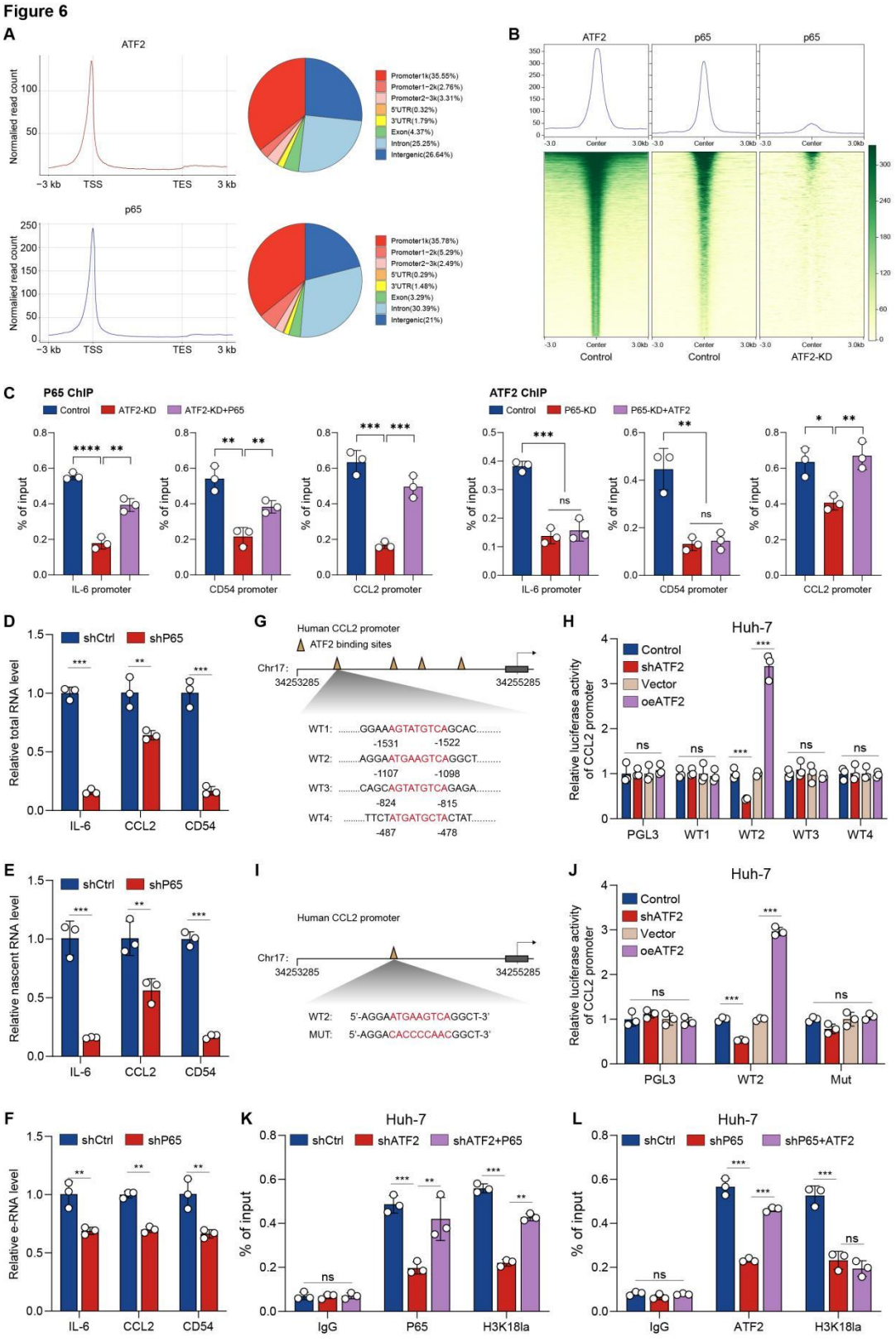


Figure 6. ATF2 cooperates with p65 to regulate CCL2 transcription through dual mechanisms of enhancer accessibility and promoter activation. (A) ChIP-seq density plots showing the genomic distribution of ATF2 and p65 binding across

transcription start sites (TSS) and transcription end sites (TES). Pie charts on the right indicate the genomic annotation of ATF2 and p65 peaks, with promoter regions showing the highest occupancy. **(B)** Heatmaps displaying p65 chromatin occupancy in control and ATF2-knockdown (ATF2-KD) cells, demonstrating that ATF2 depletion markedly reduces p65 DNA-binding abundance across the genome. **(C)** ChIP-qPCR validation of p65 and ATF2 binding at the IL-6, CD54, and CCL2 promoters in Huh-7 cells. **(D-F)** Quantification of total RNA **(D)**, nascent RNA **(E)** and enhancer RNA (eRNA) **(F)** levels for IL-6, CD54, and CCL2 following p65 or ATF2 knockdown in Huh-7 cells. **(G)** Schematic diagram showing four putative ATF2 binding sites (P1-P4) within the human CCL2 promoter region. **(H)** Dual-luciferase reporter assays of Huh-7 cells transfected with wild-type (WT1-WT4) or control (PGL3) CCL2 promoter constructs, combined with ATF2 knockdown or overexpression. **(I-J)** Mutational analysis of the ATF2-binding motif within the WT2 promoter region in Huh-7 cells. **(K)** ChIP-qPCR showing enrichment of p65 and H3K18la at the CCL2 promoter in control and ATF2-knockdown Huh-7 cells. **(L)** ChIP-qPCR analysis showing enrichment of ATF2, p65, and H3K18la in control and p65-knockdown Huh-7 cells. Data are shown as mean ± SEM; Statistical significance was determined by two-tailed Student's t-test for two-group comparisons and one-way ANOVA followed by Tukey's multiple-comparisons test for comparisons among multiple groups (*P < 0.05, **P < 0.01, ***P < 0.001).

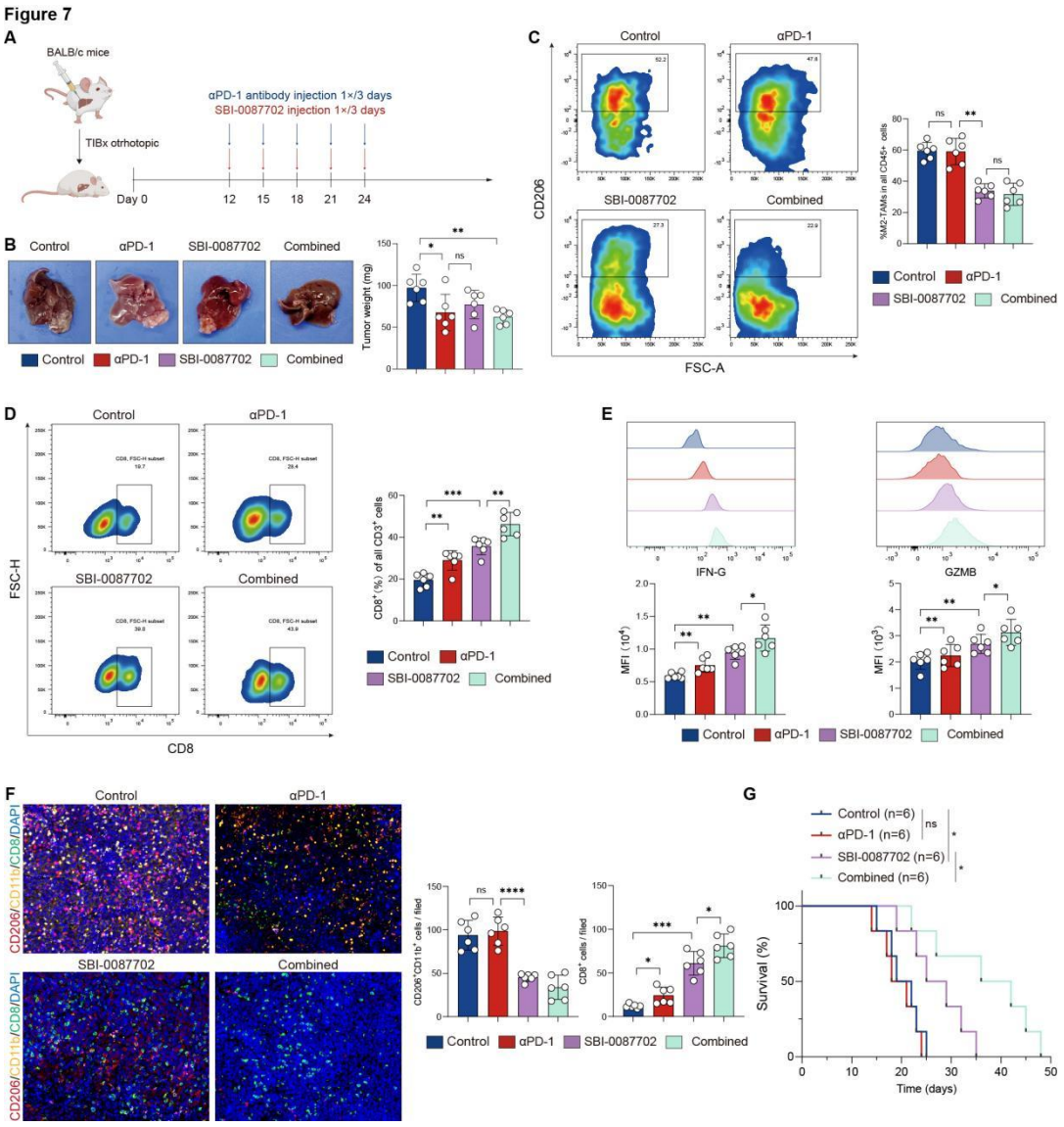


Figure 7. Pharmacological inhibition of ATF2 synergizes with αPD-1 therapy to enhance antitumor immunity in HCC. (A) Schematic of the experimental design for the orthotopic TIBx HCC model in BALB/c mice. Mice were treated with αPD-1 antibody (10 mg/kg, intraperitoneally, every 3 days) and/or the ATF2 inhibitor SBI-0087702 (25 mg/kg, intraperitoneally, every 3 days). **(B)** Representative liver images and quantification of tumor weights from each treatment group. **(C)** Flow cytometric analysis of tumor-infiltrating macrophages showing $CD206^+$ (M2-like) and $CD86^+$ (M1-like) populations. **(D)** Flow cytometry plots and quantification of $CD8^+$ T cells among total $CD3^+$ cells in tumor tissues. **(E)** Representative histograms and quantification of intracellular IFN-γ and GZMB expression in intratumoral $CD8^+$ T cells, as determined by flow cytometry. **(F)** Immunofluorescence staining of tumor

sections showing CD206⁺ macrophages (red), CD8⁺ T cells (green), and DAPI (blue). **(G)** Kaplan-Meier survival curves showing that mice receiving combined SBI-0087702 and αPD-1 treatment exhibited the longest survival compared with control, αPD-1, or SBI-0087702 monotherapy groups. Data are shown as mean ± SEM; Statistical significance was determined by two-tailed Student's t-test for two-group comparisons and one-way ANOVA followed by Tukey's multiple-comparisons test for comparisons among multiple groups (*P < 0.05, **P < 0.01, ***P < 0.001).

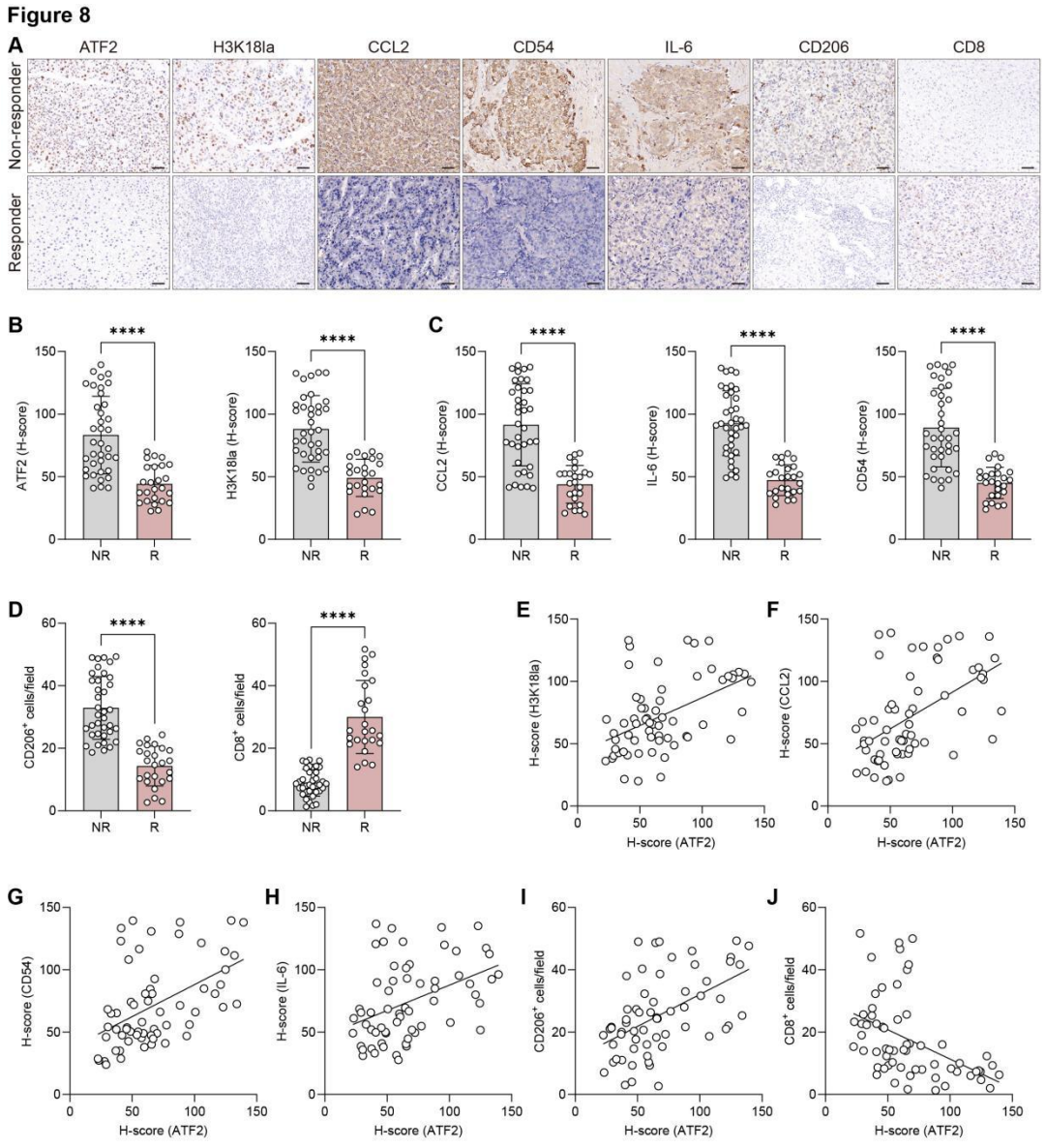
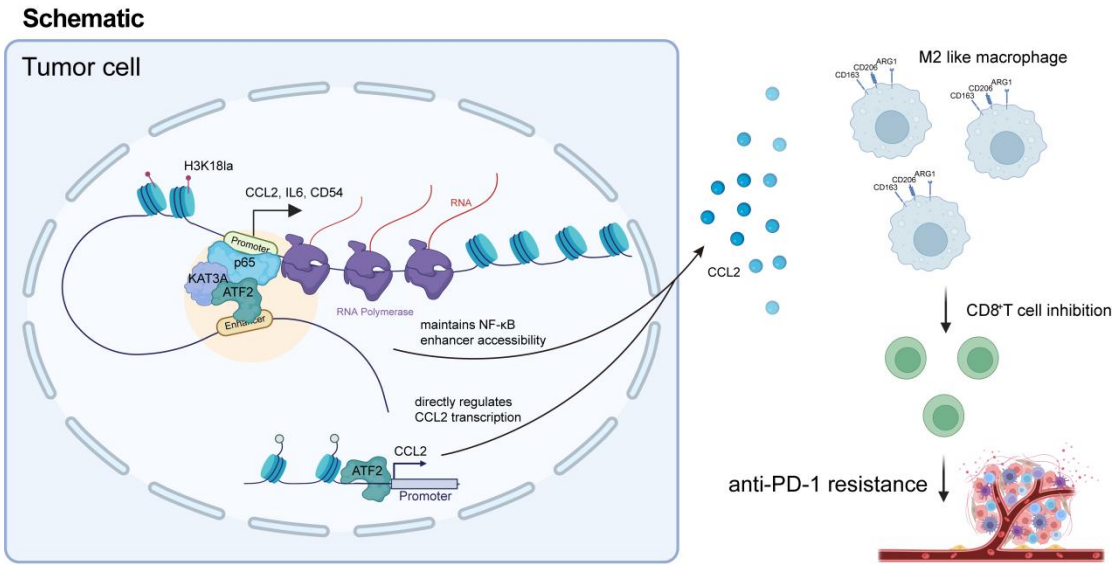


Figure 8. ATF2-associated H3K18 lactylation and NF-κB inflammatory /

chemokine target activation correlate with anti-PD-1 non-response and an immunosuppressive tumor microenvironment in HCC patients. (A) Representative immunohistochemical staining of ATF2, H3K18la, CCL2, CD54, IL-6, CD206, and CD8 in tumor specimens from anti-PD-1 non-responders and responders with HCC. Scale bars, 50 μm. **(B)** Quantification of ATF2 and H3K18la H-scores in non-responders and responders. **(C)** Quantification of H-scores for representative ATF2-associated NF-κB inflammatory/chemokine targets, including CCL2, IL-6, and CD54, in non-responders and responders. **(D)** Quantification of $CD206^+$ and $CD8^+$ cells per field in non-responders and responders. **(E-J)** Correlation analyses between ATF2 H-score and H3K18la H-score **(E)**, CCL2 H-score **(F)**, CD54 H-score **(G)**, IL-6 H-score **(H)**, $CD206^+$ cell density **(I)**, and $CD8^+$ cell density **(J)** in HCC tumor specimens. Lines indicate linear regression fits. NR, non-responder; R, responder. Data are shown as mean ± SEM; Statistical significance was determined by two-tailed Student's t-test for two-group comparisons and one-way ANOVA followed by Tukey's multiple-comparisons test for comparisons among multiple groups (*P < 0.05, **P < 0.01, ***P < 0.001).



Schematic model of the ATF2-KAT3A-H3K18la-NF-κB-CCL2 axis driving macrophage-mediated resistance to anti-PD-1 therapy in HCC. In hepatocellular

carcinoma cells, ATF2 cooperates with KAT3A/CBP to promote H3K18 lactylation and maintain chromatin accessibility at NF-κB-responsive regulatory elements, thereby sustaining p65-dependent activation of inflammatory and chemokine programs. ATF2 also directly binds the CCL2 promoter and enhances CCL2 transcription. Increased tumor-derived CCL2 promotes macrophage recruitment and M2-like polarization. These immunosuppressive macrophages restrain $CD8^+$ T-cell infiltration and effector function, leading to an immune-suppressive tumor microenvironment and resistance to anti-PD-1 therapy. Together, this model illustrates how tumor-intrinsic ATF2 couples epigenetic remodeling with chemokine signaling to promote macrophage-driven immune evasion in HCC.

Supplementary Files

This is a list of supplementary files associated with this preprint. Click to download.

- Supplementarymaterials.pdf
- Uncropedoriginalwesternblots.pdf
- SupplementaryTableS2shRNAsgRNAandsiRNAsequencesusedinthisstudy.xlsx
- SupplementaryTableS1Primersequencesusedinthisstudy.xlsx